

Article

Synthesis of Mesoporous $Zn_{1-x}M_xAl_2O_4$ Substituted by Co^{2+} and Ni^{2+} Ions and Application in the Photodegradation of Rhodamine B

Nilson Machado Pontes do Nascimento ^{1,2}, Bárbara Ronara Machado de Lima ^{1,2},
José Roberto Zamian ^{1,2}, Carlos Emmerson Ferreira da Costa ^{1,3},
Luís Adriano Santos do Nascimento ^{1,3,4} , Rafael Luque ⁵  and
Geraldo Narciso da Rocha Filho ^{1,2,3,*} 

¹ Graduation Program in Chemistry, Federal University of Pará, Augusto Corrêa Street, Guamá, Belém-PA 66075-110, Brazil; nilson-pontes@hotmail.com (N.M.P.d.N.); barbararonara@hotmail.com (B.R.M.d.L.); zamian@ufpa.br (J.R.Z.); emmersoncosta@yahoo.com.br (C.E.F.d.C.); adrlui1@yahoo.com.br (L.A.S.d.N.)

² Laboratory of Catalysis and Oilchemistry, Federal University of Pará, Street Augusto Correia, Guamá, Belém-PA 66075-110, Brazil

³ Laboratory of Oils of the Amazon, Federal University of Pará, Perimetral Avenue, Guamá, Belém-PA 66075-110, Brazil

⁴ Graduation Program in Biotechnology, Federal University of Pará, Augusto Corrêa Street, Guamá, Belém-PA 66075-110, Brazil

⁵ Department of Organic Chemistry, Universidad de Córdoba, Ctra Nnal IV-A, Km 396, E14014 Córdoba, Spain; q62alsor@uco.es

* Correspondence: geraldonrf@gmail.com

Received: 6 April 2020; Accepted: 28 April 2020; Published: 6 May 2020



Abstract: A new mesoporous $Zn_{1-x}M_xAl_2O_4$ photocatalyst was prepared using the metal-chitosan complexation method with different degrees of Zn^{2+} cation substitution with cobalt and nickel ions ($M = Co^{2+}$ and Ni^{2+}). Characterization using X-ray diffraction (XRD), Infrared absorption spectrometry (FTIR), energy dispersion spectroscopy (EDS), diffuse reflectance spectrometry (DRS), scanning electron microscopy (SEM), transmission electron microscopy (TEM), N_2 adsorption-desorption isotherms using the Barrett-Joyner-Halenda (BJH) method, thermogravimetric analysis (TG) and differential thermal analysis (DTA) confirmed the formation of the spinel phase and high purity for all samples. N_2 adsorption/desorption and size pore distribution confirmed the high surface area. The photocatalytic activity of $Zn_{1-x}M_xAl_2O_4$ and the effect of replacing Zn^{2+} ions with Ni^{2+} and Co^{2+} on the degradation of rhodamine B under ultraviolet light were studied in detail. The sample containing 0.1 mol of cobalt had the highest removal rate reaching 83%, favored by surface area and material bandgap (109 $m^2 g^{-1}$ and 2.19 eV, respectively).

Keywords: zinc aluminate; spinel; photocatalysis; chitosan

1. Introduction

Human activities produce large amounts of contaminants including oils, greases, dyes, pesticides, among others, causing serious problems to the population, compromising the air, soil and groundwater qualities [1,2]. Industrial effluents, such as those from the textile industry, may contain organic molecules that cause environmental pollution [2]. The development of methodologies for environmental remediation has received significant attention in recent years [1]. Chen and collaborators [1] used the adsorption process for the remediation of waters, utilizing a new adsorbent system from organosilica

nanoparticles with adjusted composition for the removal of anionic or cationic dyes with high adsorption capacity and fast adsorption. Liu and collaborators [3] combined the photocatalytic and adsorbent properties of core-shell Cu-BTC@TiO₂ microspheres to improve performance in the adsorptive desulfurization of thiophenic compounds from fuels under UV irradiation. While the TiO₂ layer on the surface of Cu-BTC promoted the photocatalytic oxidation of S thiophenic compounds, Cu-BTC adsorbed such oxidation products (sulfoxides and sulfones). The proposed desulfurization mechanism and the synergistic effect of Cu-BTC (as an adsorbent) and TiO₂ (as a catalyst), which capture hydroxyl radicals/activate molecules, contributed to the efficient transfer of photo-excited electrons and oxidation.

In this context, semiconductor photocatalysis emerged as a technology capable of assisting in several processes, including the degradation of organic pollutants [4–9]. Compounds with crystalline structure similar to spinel have received significant attention in applications in photocatalysis, due to their semiconductor properties, and besides being non-toxic, they have high thermal stability, resistance in acid and basic media and high surface area, among other properties [10,11].

Spinel is a ternary oxide of binary transition metals and may have a varied structure of general formula AB₂O₄, where A corresponds to bivalent cations and B to trivalent cations. In normal spinel, A²⁺ ions occupy the tetrahedral sites surrounded by four O²⁻ ions, while B³⁺ ions occupy the octahedral sites surrounded by six O²⁻ ions. The inverse spinel has the tetrahedral sites occupied by B³⁺ ions, while the octahedral sites are occupied by equal numbers of A²⁺ and B³⁺ ions with general formula (B)[AB]O₄, where the parenthesis cations are located at the tetrahedral, and the cations in brackets are in the octahedral sites. Finally, there is the intermediate spinel of the general formula, (A_{1-x}B_x)[A_xB_{2-x}]O₄, where x represents the conversion factor from one spinel to another [9,10,12–14].

Lattice enthalpy calculations based on simple ionic models indicate that for A²⁺ and B³⁺ ions the normal spinel structure is preferred, inducing greater lattice stability; however, some spinel-like structures, especially involving the block metal cations, do not meet this expectation and have been related to the stabilizing energy effect of the ligand field at the ion preference. Several spinel-like semiconductor materials have been tested in photocatalytic processes, demonstrating high activity in the photodegradation of organic pollutants [4–9,15].

For example, Hassanzadeh-Tabrizi and colleagues [16] synthesized copper aluminate, CuAl₂O₄, at much lower temperatures when using the co-precipitation method, also obtaining excellent results regarding the photocatalytic activities of methyl orange degradation, reaching approximately 90% in just 1 h of radiation exposure. Furthermore, in order to investigate the photodegradation of methyl orange under visible light, but this time modifying the synthesis methodology, Yanyan and colleagues [17] synthesized CuAl₂O₄ using the sol-gel method and achieved an impressive 97% degradation in 120 min of reaction.

Cobalt aluminate was also studied by Khademolhoseini and Talebi [9] as a catalyst in the degradation reaction of methyl orange under ultraviolet light, achieving 68% efficiency in 60 min of reaction.

ZnAl₂O₄ has received significant attention among spinel materials, being widely used as catalyst and catalyst support [11,15]. There are a variety of works developed using pure zinc aluminate in photocatalytic processes. For example, ZnAl₂O₄ has been applied in the degradation of pollutants including direct black 38 [15], reactive red 141 [18], phenol [15] and toluene gas [19], among others.

The structural properties of materials for catalytic purposes such as crystalline phase, crystallite size, surface area and average pore distribution are of great importance, as the increase of these properties produces greater contact of the active phase. Commercial zinc aluminate has a low surface area and low pore volume, characteristics that make contact with the material to be degraded and the photocatalyst less favorable. However, obtaining this material by different synthesis routes has significantly improved its properties, thus allowing it to be used with greater efficiency in photocatalysis [16,18–22].

ZnAl₂O₄ has a wide bandgap, making it suitable for photocatalytic applications in the ultraviolet range. However, several studies have reported that the ZnAl₂O₄ bandgap changes according to the synthesis method employed. Battiston et al. [10] reported a bandgap equal to 3.8 eV for ZnAl₂O₄ synthesized via the co-precipitation method. Anand, Kennedy and Vijaya [12] for the same material, produced using the microwave combustion method, obtained a bandgap equal to 5.01 eV. Yanyan et al. [17] produced ZnAl₂O₄ via the sol-gel synthesis route with bandgap values of 3.25 and 3.33 eV. In the literature, few studies have been developed and published in order to evaluate the influence that metal doping has on its final photocatalytic activity [10,23].

According to the above, this research was aimed to prepare ZnAl₂O₄ using the metal-chitosan complexation method with partial replacement of Zn²⁺ by Co²⁺ and Ni²⁺, producing a new mesoporous catalyst with high surface area. In addition, we investigated for the first time the photocatalytic activity of mesoporous Zn_{1-x}M_xAl₂O₄ synthesized using metal-chitosan complexation and the effect of replacing Zn²⁺ ions with Ni²⁺ and Co²⁺ on the degradation of rhodamine B under ultraviolet light irradiation. Ni²⁺ and Co²⁺ ions were prioritized for the replacement of zinc in the structure of ZnAl₂O₄, due to their periodic properties. Both ions have coordination 4 and 6, in addition to having an ionic radius similar to each other, which favors substitution.

2. Experimental

2.1. Reagents

The reagents used for the synthesis of photocatalysts present in this work were not subjected to any purification treatment and were all of analytical grade and high purity: chitosan (Sigma-Aldrich, St. Louis, MO, USA), acetic acid (99.8%, Neon, Suzano, São Paulo, Brazil), Zn(NO₃)₂·6H₂O (96%, Dinâmica, Indaiatuba, São Paulo, Brazil), Al(NO₃)₃·9H₂O (98%, Dinâmica, Indaiatuba, São Paulo, Brazil) and NH₄OH (28–30%, Dinâmica, Indaiatuba, São Paulo, Brazil).

To obtain 2.0 g of the sample of zinc aluminate (ZnAl₂O₄), initially 2.5 g of chitosan were dissolved in 100 mL of acetic acid solution (5% v/v), under stirring. Then, two solutions were prepared: 3.02 g of Zn(NO₃)₂·6H₂O was dissolved in 5.08 mL of distilled water and 8.0 g of Al(NO₃)₃·9H₂O was dissolved in 7.62 mL of distilled water. Subsequently, the two solutions formed using Al and Zn were added dropwise to the chitosan solution under constant stirring, after which the mixture was stirred for 1 h. The resulting Zn-Al-chitosan solution (at a 1:2:1.5 molar ratio) was added dropwise in 50 mL, 50% v/v NH₄OH, adjusting the pH of the solution to remain in 9.0 ± 0.5, stirring for 3 h until complete homogenization.

Spheres consisting of a chitosan complex with the metal hydroxides of Zn²⁺ and Al³⁺ were observed, filtered and washed with distilled water. They were then dried at room temperature for 48 h. They were calcined for 4 h at different temperatures (550, 650, 750, 850 and 950 °C) to eliminate residual organic matter and spinel formation. After this process, the formed product was slowly cooled to room temperature.

The synthesis of zinc aluminates substituted using Ni²⁺ and Co²⁺ metal ions followed the same methodology; however, the precursor salts of the metals were added in specific theoretical stoichiometric proportions in order to obtain the samples in the desired theoretical molar ratio [21,24,25].

2.2. Characterization of Synthesized Materials

X-ray diffractograms were obtained using the D8 BRUKER (Madison, WI, USA) powder diffractometer method using CuK α radiation (0.15406 nm) at a scan rate of 0.02 °/min, the voltage and current of the tube were 40 kV and 40 mA, respectively. Infrared analysis with Fourier transform was performed using the KBr pellet method in the region of 900 to 400 cm⁻¹ using BRUKER VERTEX 70 v equipment.

The morphological characteristics were evaluated using a TESCAN scanning electron microscope model VEGA3 (Fuveau, Village of Provence, France), with an electron beam current in the

range of 85–90 μA , and transmission electron microscopy, with a TEM FEI Tecnai G2T20 device (Milan, Lombardy, Italy).

Surface area, diameter and pore volume were calculated according to the Brunauer-Emmett-Teller and Barret-Joyner-Halenda (BET/BJH) methods using a Micromeritics Vacprep 061 Sample Degas System (Norcross, GA, USA). The samples were subjected to a pre-treatment for degassing of 200 °C for 2 h. Sample composition was determined on an X-ray fluorescence spectrometer (EDX-700, Shimadzu, Barueri, São Paulo, Brazil).

Thermal analysis was performed at a temperature range of 24 to 1000 °C in a platinum crucible with a heating rate of 10 °C min^{-1} and gas flow of 50 mL min^{-1} in a SHIMADZU Differential Thermal Analysis (DTA) and Differential Thermogravimetry (DTG) apparatus thermal analyzer (Barueri, São Paulo, Brazil).

Diffuse reflectance spectrometry was performed on Shimadzu UV-2600 equipment (Barueri, São Paulo, Brazil), and measurements of the band gap reflectance and photon energy spectra were performed on Shimadzu ISR-2600 Plus equipment with integration spheres from the standard of barium sulphate.

2.3. Photocatalytic Performance

The synthesized materials were evaluated for the degradation of rhodamine B under ultraviolet radiation (320–280 nm) from a 9-watt mercury lamp. First, 100 mg of photocatalyst was dispersed in a 100 mL solution of dye with an initial concentration of 10 mg L^{-1} . The suspension formed was initially kept in the dark for half an hour under agitation and aeration to achieve the adsorption and desorption equilibrium. Aliquots were collected at 30 min intervals and then centrifuged. For these samples, the absorbance was read on a UV-visible spectrophotometer (Thermo Scientific, Evolution array UV-visible spectrophotometer) (Waltham, MA, USA) at a wavelength of 553 nm [26].

3. Results and Discussion

3.1. X-Ray Diffraction (XRD)

The diffractograms for the ZnAl_2O_4 samples treated at temperatures from 550 °C to 950 °C are shown in Figure 1. All peaks analyzed could be indexed in the center face cubic structure of ZnAl_2O_4 according to JCPDS No. 01-071-0968, which have the following 2θ angles: 31.2°, 36.8°, 44.8°, 49.1°, 55.7°, 59.6°, 65.2°, 74.1° and 77.3°, corresponding to the crystallographic planes (220), (311), (400), (422), (511), (440), (620) and (533), respectively. The diffraction patterns of the prepared materials are also very similar to those presented by Stringhini et al. [25] and Zhu et al. [27]. The increase in the synthesis temperature caused an increase in the crystallinity of the samples, characterized by an increase in peak intensity and narrowing of the width by half height, which may be associated with the average size of the crystallite.

The diffractograms for the cobalt-substituted zinc aluminate samples $\text{Co}_x\text{Zn}_{1-x}\text{Al}_2\text{O}_4$ ($x = 0.1, 0.5, 0.9$ e 1.0 mol) calcined at 750 °C are shown in Figure 1b; the increase in the substitution of Zn^{2+} ions present in the spinel structure caused a decrease in the intensity of the peaks, indicating a decrease in the crystallinity of the synthesized material, within the employed conditions. When analyzing the network parameter in relation to the degree of substitution of the Zn^{2+} ions in the structure of the zinc aluminate, the lattice parameter increases as the replacement of the ions occurs, since the Co^{2+} ions are larger than the ions Zn^{2+} , thus producing larger particles [5,12,13]. All studied x -values were indexed according to JCPDS N 01-082-2252 for CoAl_2O_4 . XRD standards for the $\text{Ni}_x\text{Zn}_{1-x}\text{Al}_2\text{O}_4$ ($x = 0.1, 0.5, 0.9$ e 1.0 mol) samples calcined at 950 °C are shown in Figure 1c. For all studied x -values the characteristic spinel phase peaks detected were perfectly indexed according to JCPDS N 01-078-1601 for NiAl_2O_4 . According to X-ray patterns, no intermediate phase or impurity was observed at any of the proposed x -values; however, at lower temperatures a mixture of NiO and NiAl_2O_4 is formed and the spinel phase is not obtained, so this temperature was prioritized for the calcination process of

samples replaced by Ni^{2+} ions. However, the increased substitution of zinc ions caused a decrease in peak intensity.

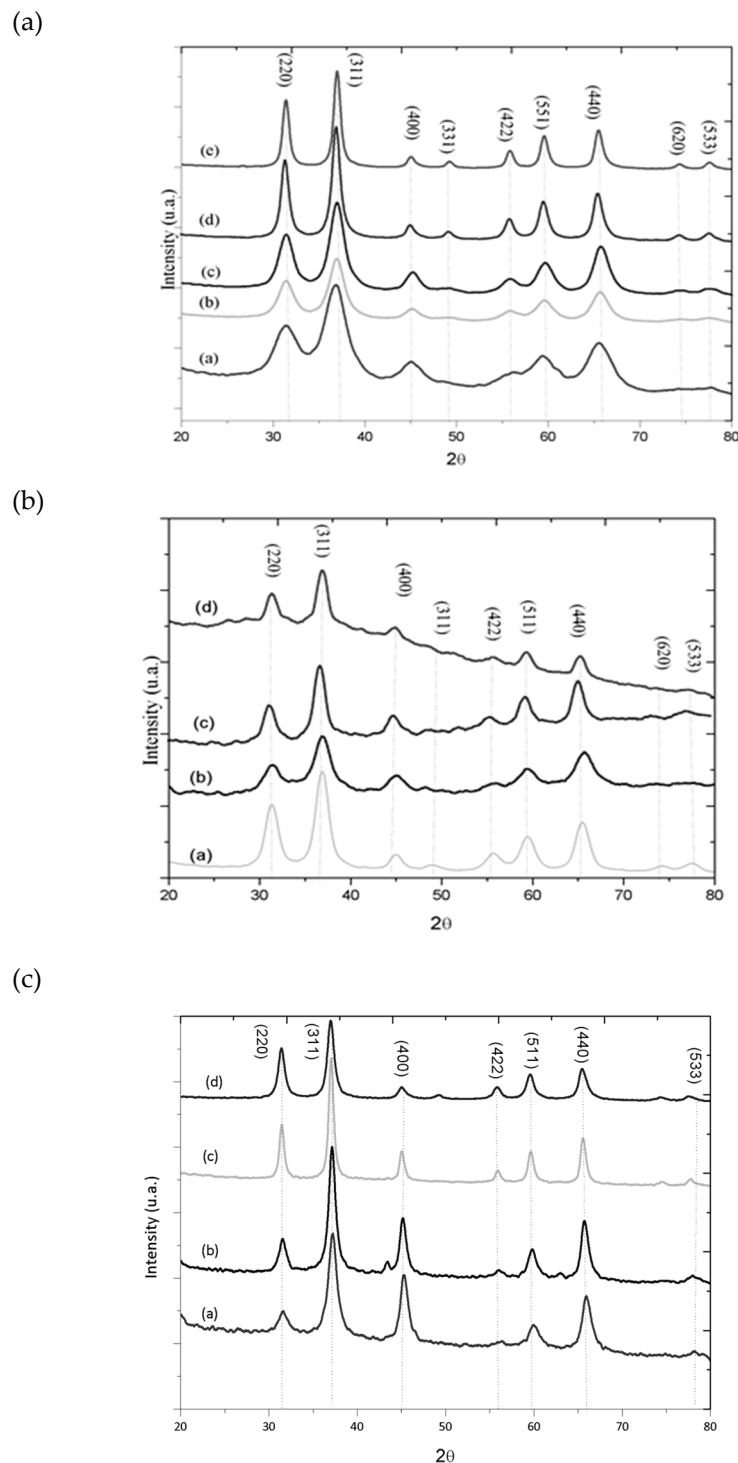


Figure 1. X-ray diffractograms of the samples obtained using the metal-chitosan complexation method: (a)—(a) ZnAl_2O_4 -550, (b) ZnAl_2O_4 -650, (c) ZnAl_2O_4 -750, (d) ZnAl_2O_4 -850, (e) ZnAl_2O_4 -950; (b)—(a) $\text{Co}_{0.1}\text{Zn}_{0.9}\text{Al}_2\text{O}_4$ -750, (b) $\text{Co}_{0.5}\text{Zn}_{0.5}\text{Al}_2\text{O}_4$ -750, (c) $\text{Co}_{0.1}\text{Zn}_{0.9}\text{Al}_2\text{O}_4$ -750, (d) $\text{CoZnAl}_2\text{O}_4$ -750; (c)—(a) NiAl_2O_4 -950, (b) $\text{Ni}_{0.9}\text{Zn}_{0.1}\text{Al}_2\text{O}_4$ -950, (c) $\text{Ni}_{0.5}\text{Zn}_{0.5}\text{Al}_2\text{O}_4$ -950, (d) $\text{Ni}_{0.1}\text{Zn}_{0.9}\text{Al}_2\text{O}_4$ -950.

It can be observed that while Zn^{2+} ions were replaced by Ni^{2+} ions, the lattice parameter decreased, ranging from 8.063 to 8.018 Å; similar behavior was described by Han et al. [28]. Porta, Anichini and

Bucciarelli [29] observed the same tendency when evaluating the effect of replacing Zn^{2+} ions of zinc aluminate with Ni^{2+} ions, which obtained values ranging from 8.0874 Å, for the pure zinc aluminate sample at 8.0509 Å when the ions were completely replaced.

Kapase et al. [5], Anand et al. [12] and Ianos et al. [30] obtained similar values for the pure $ZnAl_2O_4$ lattice parameter of respectively 8.081, 8.0747 and 8.089 Å. While for the $NiAl_2O_4$ lattice parameter, Dhak and Pramanik [31] obtained 8.0285 Å, Gama et al. [32] obtained from 8.048 Å and Porta, Stone and Turner [33] 8.0514 Å. With this decrease there was a consequent reduction of the unit cell volume from 524 to 516 Å³. The lattice parameters and unit cell volumes for all samples are presented in Table 1. For pure zinc aluminate, as the calcination temperature increased, the lattice parameter decreases from 8.124 Å to 8.064 Å.

Table 1. Bandgap, lattice parameter and unit cell volume for samples $Zn_{1-x}M_xAl_2O_4$.

| Sample | Bandgap (eV) | Lattice Parameter, a (Å) | Unit Cell Volume, a ³ , (Å ³) |
|--------------------------------|--------------|--------------------------|--|
| $ZnAl_2O_4$ -550 | 3.30 | 8.124 | 536 |
| $ZnAl_2O_4$ -650 | 3.04 | 8.080 | 528 |
| $ZnAl_2O_4$ -750 | 3.16 | 8.070 | 526 |
| $ZnAl_2O_4$ -850 | 3.27 | 8.066 | 525 |
| $ZnAl_2O_4$ -950 | 3.19 | 8.064 | 524 |
| $Ni_{0.1}Zn_{0.9}Al_2O_4$ -950 | 2.98 | 8.060 | 524 |
| $Ni_{0.5}Zn_{0.5}Al_2O_4$ -950 | 3.20 | 8.034 | 519 |
| $Ni_{0.9}Zn_{0.1}Al_2O_4$ -950 | 2.78 | 8.031 | 518 |
| $NiAl_2O_4$ -950 | 3.12 | 8.018 | 516 |
| $Co_{0.1}Zn_{0.9}Al_2O_4$ -750 | 2.19 | 8.074 | 526 |
| $Co_{0.5}Zn_{0.5}Al_2O_4$ -750 | 2.21 | 8.088 | 529 |
| $Co_{0.9}Zn_{0.1}Al_2O_4$ -750 | 2.51 | 8.091 | 530 |
| $CoAl_2O_4$ -750 | 3.90 | 8.103 | 532 |

3.2. Diffuse Reflectance Spectrometry

The bandgap of $ZnAl_2O_4$ samples, available in Table 1 (see also Figure S1), showed values of approximately 3.20 eV for unsubstituted samples. The metal-chitosan complexation method produced a material with a smaller energy gap. Therefore, it can be considered that the synthesis method significantly changes the bandgap of the materials.

In the process of replacing Zn^{2+} ions with Ni^{2+} , the band interval showed values of 3.12 eV for the fully replaced sample ($NiAl_2O_4$ -950) and 3.20 eV for the $Ni_{0.5}Zn_{0.5}Al_2O_4$ -950 sample, showing no major changes compared to the unsubstituted sample ($ZnAl_2O_4$ -950). The decrease in the bandgap value is associated with the amount of ions that were replaced, in the proportion of 0.1:0.9, with ions in the amount of 0.1 acting as doping of $ZnAl_2O_4$ by the ions Ni^{2+} and Co^{2+} . The difference in the dopant's electronic structure causes a decrease in the bandgap value [12]. The same effect occurs in the replacement of nickel ions in $NiAl_2O_4$. In samples replaced by cobalt ions, the bandgap value increased as the amount of cobalt ions increases. For $Co_{0.1}Zn_{0.9}Al_2O_4$ -750, the bandgap varied from 2.19 to 3.90 eV when the Zn^{2+} ions were completely replaced; similar values of bandgap were reported by Anand, Kennedy and Vijaya [12].

3.3. Infrared Absorption Spectroscopy

Figure 2 shows the infrared spectrum with Fourier transform (FT-IR) for the synthesized samples. Spinel is characterized by having three bands in the 800 to 450 cm^{-1} range, which confirms the formation of the structure, as these bands are typical of interactions between Al-O at octahedral sites and Zn-O at tetrahedral sites [12,25,34]. The bands located in the 400 to 500 cm^{-1} range are characteristic of the vibrations referring to the interactions between metals and oxygen occupying octahedral sites, and the bands in the 550 to 700 cm^{-1} range are characteristic bands of the vibrations between the metal and oxygen occupying tetrahedral sites [15]. In Figure 2a, vibrations close to ~ 494 cm^{-1} can

be attributed to the vibrations of the group $[Al^{3+}O_6]$ occupying the octahedral sites, and the bands $\sim 680\text{ cm}^{-1}$ and $\sim 570\text{ cm}^{-1}$ are typical of Zn-O connections occupying the tetrahedral sites. The formed material presents a normal spinel structure, due to the absence of vibrations $\sim 730\text{ cm}^{-1}$ referring to interaction ($Al^{3+}O_4$) at the tetragonal sites [6,12].

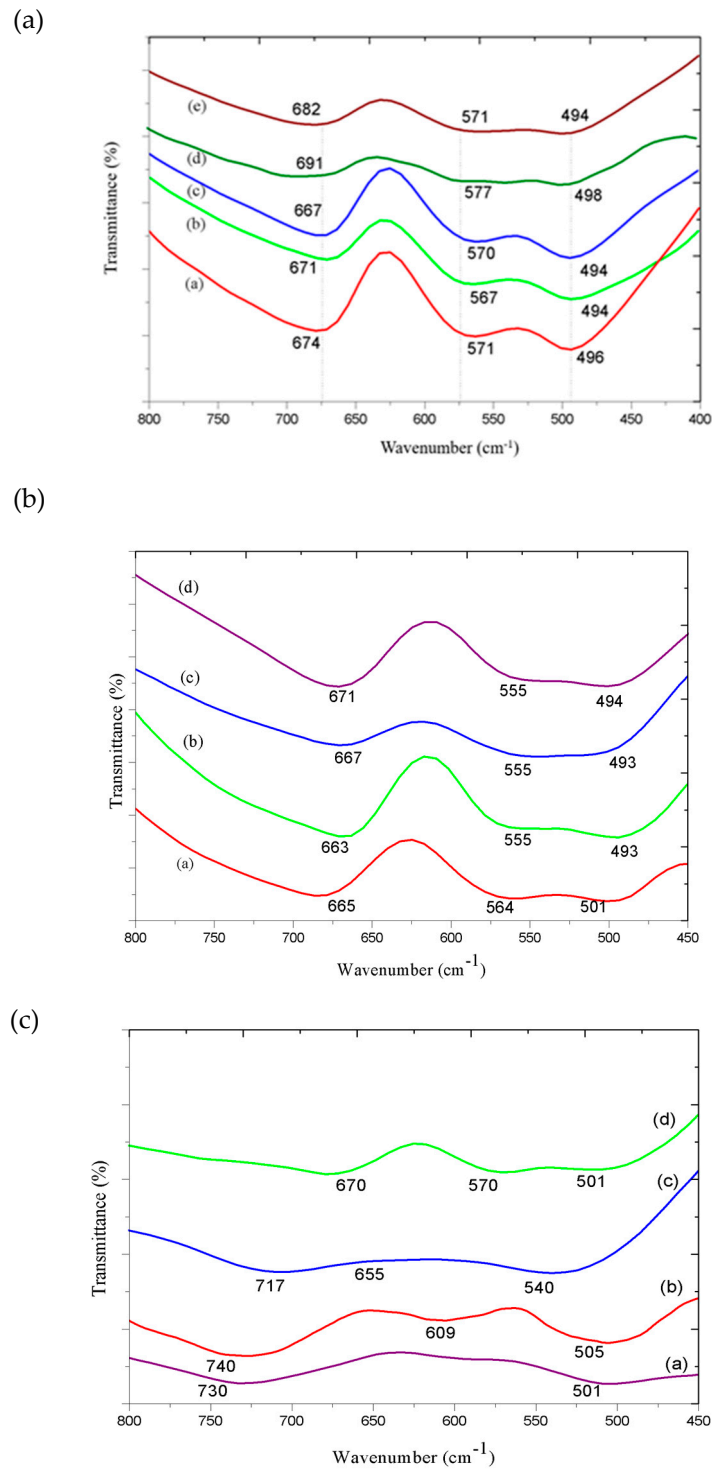


Figure 2. Infrared with Fourier transform of the samples obtained using the metal-chitosan complexation method: (a)—(a) $ZnAl_2O_4$ -550, (b) $ZnAl_2O_4$ -650, (c) $ZnAl_2O_4$ -750, (d) $ZnAl_2O_4$ -850, (e) $ZnAl_2O_4$ -950; (b)—(a) $CoAl_2O_4$ -750, (b) $Co_{0.9}Zn_{0.1}Al_2O_4$ -750, (c) $Co_{0.5}Zn_{0.5}Al_2O_4$ -750, (d) $Co_{0.1}Zn_{0.9}Al_2O_4$ -750; (c)—(a) $NiAl_2O_4$ -950, (b) $Ni_{0.9}Zn_{0.1}Al_2O_4$ -950, (c) $Ni_{0.5}Zn_{0.5}Al_2O_4$ -950, (d) $Ni_{0.1}Zn_{0.9}Al_2O_4$ -950.

The spectra of the samples replaced by Co^{2+} ions, Figure 2b, presented the vibrational modes in about ~ 670 , ~ 560 and $\sim 494 \text{ cm}^{-1}$. The vibrations at $\sim 494 \text{ cm}^{-1}$ are attributed to the vibrations of Al^{3+} ions occupying octahedral sites [Al^{3+}O_6], while the bands at ~ 670 and $\sim 560 \text{ cm}^{-1}$ are attributed to the tetrahedral sites being occupied by the Zn^{2+} and Co^{2+} ions ($\text{Zn}^{2+}\text{O}_4:\text{Co}^{2+}\text{O}_4$), confirming the formation of the spinel phase for the replaced samples, being classified as normal spinel [11,30].

The spectra of the samples replaced by Ni^{2+} ions, Figure 2c, showed vibrational modes characteristic of the spinel phase in the region of ~ 497 , 560 and 650 cm^{-1} , thus confirming the formation of the normal spinel phase for the sample $\text{Ni}_{0.1}\text{Zn}_{0.9}\text{Al}_2\text{O}_4$ -950; however, the $\text{Zn}_{1-x}\text{Ni}_x\text{Al}_2\text{O}_4$ samples ($x = 0.5$, 0.9 and 1.0 mol) showed a vibration around $\sim 730 \text{ cm}^{-1}$ characteristic for Ni^{2+} occupying the octahedral site, and the replacement of Zn^{2+} ions by Ni^{2+} ions produced an inverted spinel.

3.4. Energy Dispersion Spectroscopy (EDS)

The chemical composition of the samples was determined using energy dispersion spectroscopy (EDS). Table 2 shows the percentages of the metal oxides obtained. Based on these data it can be concluded that the synthesized material has a high degree of purity, with an impurity range for pure ZnAl_2O_4 of from 0.08% to 0.26%.

Table 2. X-ray fluorescence spectroscopy quantification and energy dispersion spectroscopy.

| Sample Theoretical | EDX Al_2O_3 (%) | EDX Co_2O_3 (%) | EDX ZnO (%) | EDX NiO (%) | EDX Fe_2O_3 (%) | EDX CaO (%) |
|--|---------------------------------|---------------------------------|-------------|-------------|---------------------------------|-------------|
| ZnAl_2O_4 -550 | 65.8 | — | 23.7 | — | 0.08 | — |
| ZnAl_2O_4 -650 | 59.9 | — | 28.5 | — | 0.08 | 0.26 |
| ZnAl_2O_4 -750 | 63.9 | — | 24.1 | — | 0.06 | 0.11 |
| ZnAl_2O_4 -850 | 70.7 | — | 27.2 | — | 0.14 | — |
| ZnAl_2O_4 -950 | 74.0 | — | 21.8 | — | — | — |
| CoAl_2O_4 -750 | 62.2 | 32.4 | — | — | — | — |
| NiAl_2O_4 -950 | 71.3 | — | — | 25.3 | — | — |
| $\text{Co}_{0.1}\text{Zn}_{0.9}\text{Al}_2\text{O}_4$ -750 | 58.6 | 5.1 | 31.4 | — | 0.12 | 0.14 |
| $\text{Co}_{0.5}\text{Zn}_{0.5}\text{Al}_2\text{O}_4$ -750 | 50.6 | 41.3 | 15.1 | — | 0.11 | — |
| $\text{Co}_{0.9}\text{Zn}_{0.1}\text{Al}_2\text{O}_4$ -750 | 52.3 | 41.3 | 1.9 | — | — | — |
| $\text{Ni}_{0.1}\text{Zn}_{0.9}\text{Al}_2\text{O}_4$ -950 | 60.5 | — | 29.8 | 2.8 | 0.30 | 0.35 |
| $\text{Ni}_{0.5}\text{Zn}_{0.5}\text{Al}_2\text{O}_4$ -950 | 69.1 | — | 18.8 | 11.5 | 0.15 | — |
| $\text{Ni}_{0.9}\text{Zn}_{0.1}\text{Al}_2\text{O}_4$ -950 | 59.2 | — | 5.8 | 33.7 | 0.14 | — |

$\text{Co}_{0.1}\text{Zn}_{0.9}\text{Al}_2\text{O}_4$ -750 and $\text{Co}_{0.5}\text{Zn}_{0.5}\text{Al}_2\text{O}_4$ -750 showed 0.26% and 0.11% of impurities, respectively. The sample with $x = 0.9$ of cobalt ions was completely pure. For ZnAl_2O_4 replaced by 0.1 of Ni^{2+} ions, it was quantified with a total of 0.65%, while nickel ion samples 0.5 and 0.9 presented impurity of 0.15% and 0.14%, respectively. The obtained molar stoichiometry is consistent with the proposed theoretical values.

3.5. Scanning Electron Microscopy (SEM) and Transmission Electron Microscopy (TEM)

All samples produced were spherical in shape before (Figure S2) and after calcination. Samples replaced by Zn^{2+} and Co^{2+} ions exhibited a similar profile to those of pure aluminates. Therefore, SEM analyses were performed for ZnAl_2O_4 , NiAl_2O_4 and CoAl_2O_4 samples. According to the analyses, it can be concluded that the spheres formed after calcination are hollow and exhibit cracks on the surface, justifying the synthesis process based on chitosan as a template, and its elimination during calcination produces a highly porous spherical structure with low mechanical resistance. The materials have a sponge-like porosity, as shown in Figure 3b,d,f.

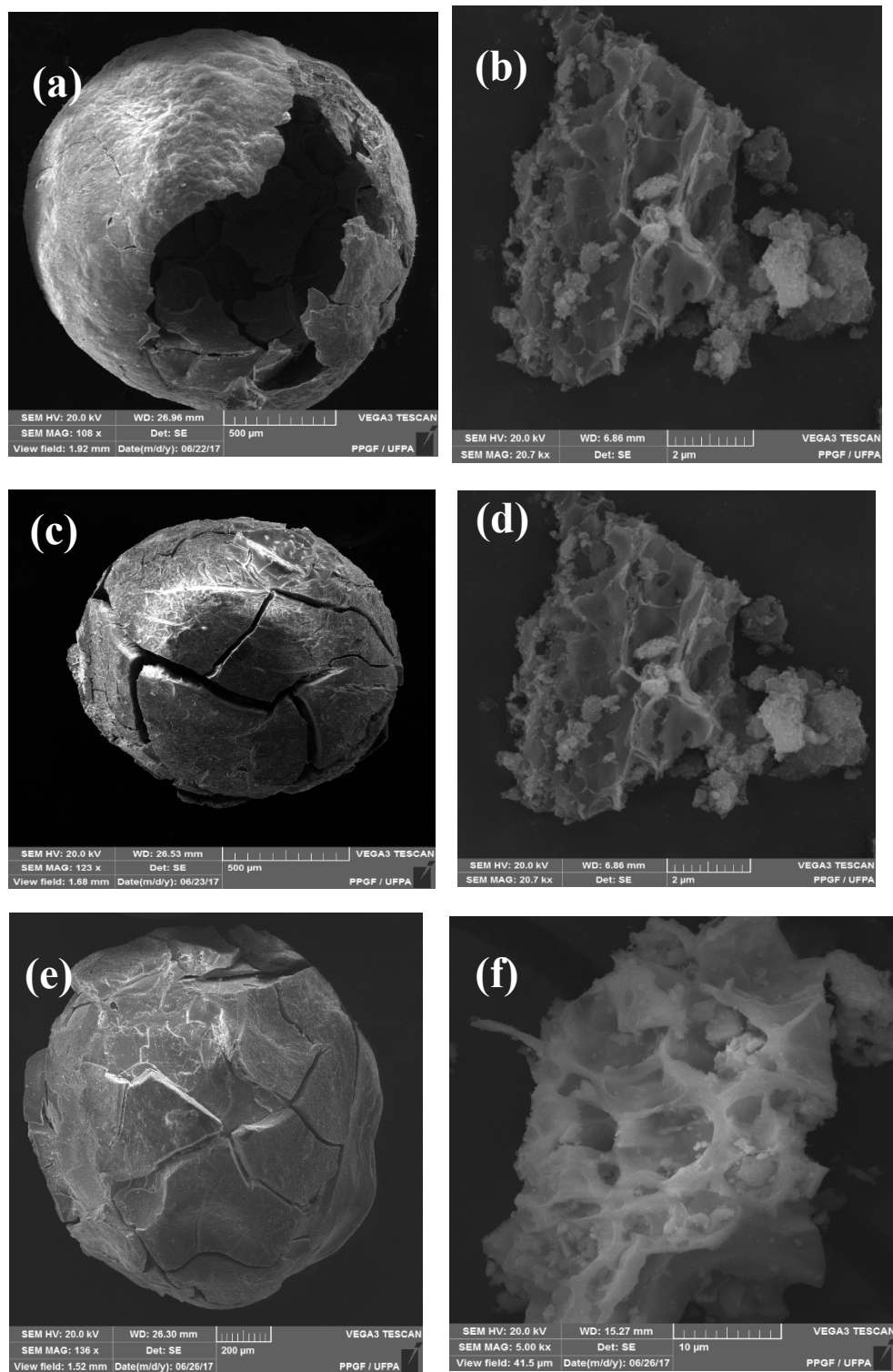


Figure 3. Scanning electron micrographs of samples (a) and (b) ZnAl_2O_4 -750; (c) and (d) NiAl_2O_4 -950; (e) and (f) CoAl_2O_4 -750.

Figure 4 shows the transmission micrographs for the ZnAl_2O_4 -750, NiAl_2O_4 -950 and CoAl_2O_4 -750 samples. The images show that the zinc, cobalt and nickel aluminate particles are uniform and nanoaggregated; The zinc metal ions using Co^{2+} and Ni^{2+} showed no significant changes in material morphology.

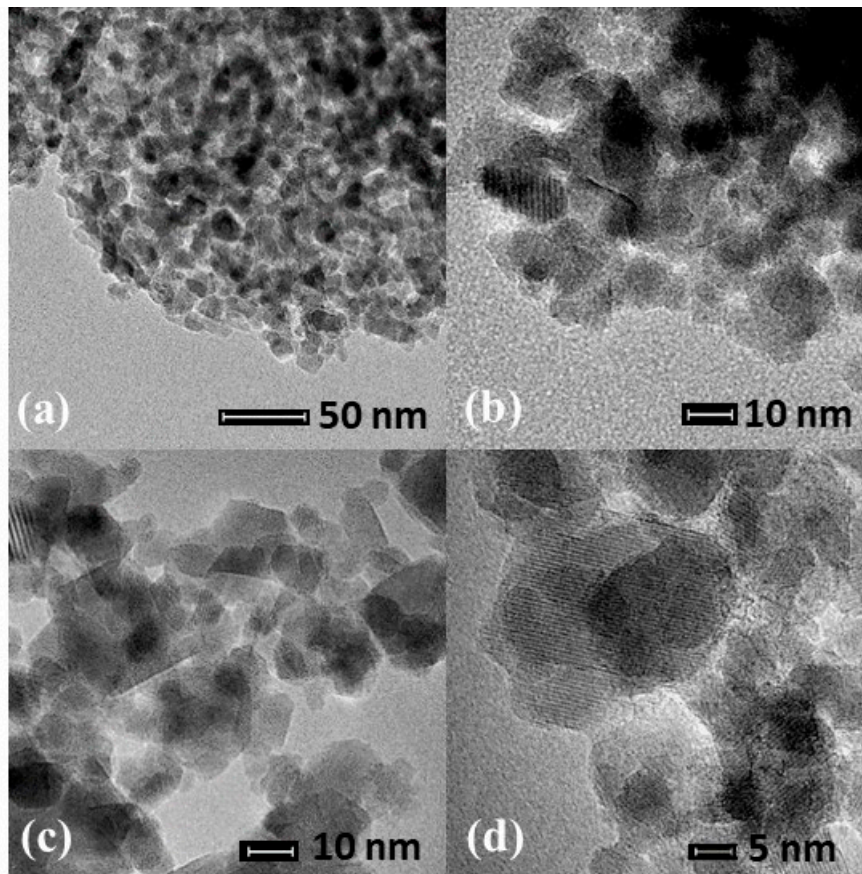


Figure 4. Transmission electron microscopy (TEM) of samples (a) ZnAl_2O_4 -750; (b) NiAl_2O_4 -950; (c) CoAl_2O_4 -750; (d) NiAl_2O_4 -950.

3.6. N_2 Adsorption-Desorption Isotherms

Adsorption-desorption isotherms of N_2 , Figure 5a–c, showed a similar profile. According to the IUPAC classification, these isotherms can be defined as type IV isotherms because they have a characteristic hysteresis cycle of mesoporous structure [35]. The mesoporosity of the samples was confirmed by analyzing the average pore size distribution using the Barrett-Joyner-Halenda (BJH) method. Average pore size distribution graphs are available in Figure 5d–f, which show a predominant distribution in the mesoporous structure region ($2 < \text{average pore size} < 50 \text{ nm}$) [22].

Figure 5d shows the average pore size distribution for the zinc aluminate samples, synthesized at a calcination temperature of 550 to 950 °C. It can be seen that they all had a unimodal distribution, with ZnAl_2O_4 -550 and ZnAl_2O_4 -950 having a narrow unimodal with pore size ranging close to 4.5 nm and 6.5 nm, respectively. The distribution is similar to that obtained by Anchieta and collaborators [15]. The samples ZnAl_2O_4 -650, ZnAl_2O_4 -750 and ZnAl_2O_4 -850 showed, however, a wide unimodal distribution, with mean pore values of 4 to 5 nm, 6.5 to 9 nm and 5 to 7 nm, respectively.

Figure 5b shows the N_2 adsorption-desorption isotherms for cobalt substituted samples at the theoretical molar ratio of 0.1, 0.5, 0.9 and 1.0; they all presented type IV isotherms similar to those obtained for unsubstituted ZnAl_2O_4 samples, which was confirmed by the analysis of the average pore size.

The replacement of Zn^{2+} ions in the structure of zinc aluminate caused changes in its textural properties. By replacing 0.1 of Zn^{2+} ions with Co^{2+} ions the surface area decreases from 175 to 109 $\text{m}^2 \text{ g}^{-1}$. Similarly, the total volume of pore size decreased from 0.331 to 0.282 $\text{cm}^3 \text{ g}^{-1}$; however, the average pore diameter increased significantly from 59.2 to 74.4 Å. According to the data obtained by

the BET/BJH analysis, the increase in the calcination temperature linearly caused a decrease in the surface area of the $ZnAl_2O_4$ samples.

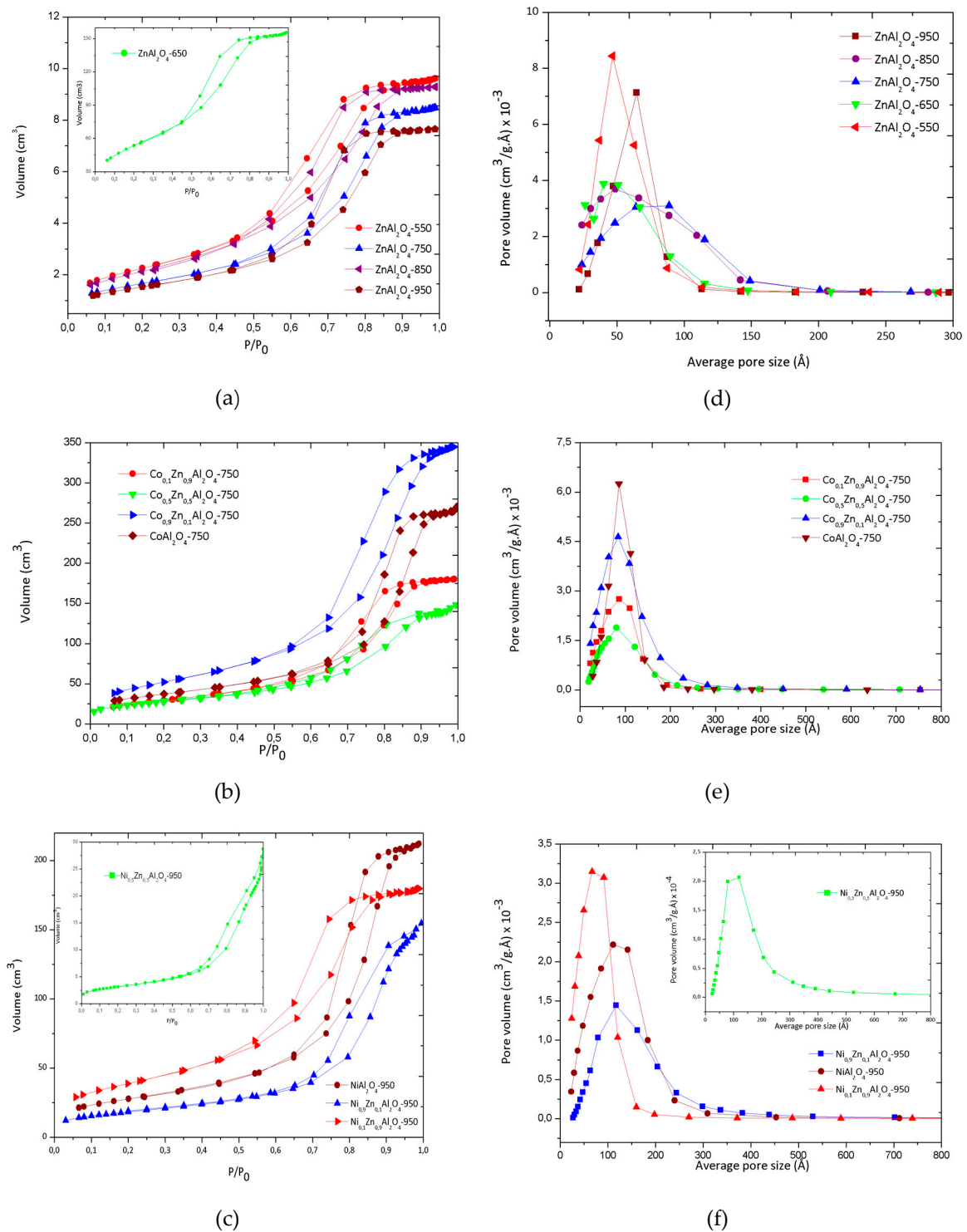


Figure 5. N_2 adsorption-desorption isotherms and average pore size distribution. N_2 adsorption-desorption isotherms for: (a) $ZnAl_2O_4$ samples, (b) samples replaced by cobalt ions. (c) samples replaced by nickel ions. Average pore size distribution for: (d) $ZnAl_2O_4$ samples, (e) samples replaced by cobalt ions, (f) samples replaced by nickel ions.

Replacing zinc ions with cobalt metal ions increased the surface area of the material to $193 \text{ m}^2 \text{ g}^{-1}$ for the sample replaced with 0.9 of Co^{2+} ions, but the CoAl_2O_4 -750 sample had an intermediate surface area of $135 \text{ m}^2 \text{ g}^{-1}$ and an average pore size of 110 \AA . Table 3 presents the data regarding surface area, average pore diameter and total pore volume for all materials obtained.

Table 3. Surface area, average pore diameter and total pore volume of samples $\text{Zn}_{1-x}\text{M}_x\text{Al}_2\text{O}_4$.

| Sample | Surface Area ($\text{m}^2 \text{ g}^{-1}$) | Average Pore Size (\AA) | Total Pore Volume ($\text{cm}^3 \text{ g}^{-1}$) |
|--|--|------------------------------------|--|
| ZnAl_2O_4 -550 | 197 | 45.9 | 0.255 |
| ZnAl_2O_4 -650 | 185 | 58.3 | 0.343 |
| ZnAl_2O_4 -750 | 175 | 59.2 | 0.331 |
| ZnAl_2O_4 -850 | 136 | 69.3 | 0.300 |
| ZnAl_2O_4 -950 | 124 | 69.3 | 0.270 |
| NiAl_2O_4 -950 | 101 | 85.4 | 0.330 |
| $\text{Ni}_{0.9}\text{Zn}_{0.1}\text{Al}_2\text{O}_4$ -950 | 67 | 129.9 | 0.234 |
| $\text{Ni}_{0.5}\text{Zn}_{0.5}\text{Al}_2\text{O}_4$ -950 | 30 | 63.0 | 0.072 |
| $\text{Ni}_{0.1}\text{Zn}_{0.9}\text{Al}_2\text{O}_4$ -950 | 141 | 78.3 | 0.285 |
| CoAl_2O_4 -750 | 135 | 85.2 | 0.421 |
| $\text{Co}_{0.9}\text{Zn}_{0.1}\text{Al}_2\text{O}_4$ -750 | 193 | 110.2 | 0.532 |
| $\text{Co}_{0.5}\text{Zn}_{0.5}\text{Al}_2\text{O}_4$ -750 | 101 | 82.0 | 0.227 |
| $\text{Co}_{0.1}\text{Zn}_{0.9}\text{Al}_2\text{O}_4$ -750 | 109 | 74.4 | 0.282 |

Replacing 0.1 of the Zn^{2+} ions in the ZnAl_2O_4 structure with Ni^{2+} ions in the $\text{Ni}_{0.1}\text{Zn}_{0.9}\text{Al}_2\text{O}_4$ -750 sample caused a significant change in their properties. The surface area decreases from $175 \text{ m}^2 \text{ g}^{-1}$ in the ZnAl_2O_4 -750 sample to $141 \text{ m}^2 \text{ g}^{-1}$, while with the replacement the mean pore diameter increased from 59.2 \AA to 78.3 \AA . However, the total pore volume decreased from $0.331 \text{ cm}^3 \text{ g}^{-1}$ to $0.285 \text{ cm}^3 \text{ g}^{-1}$.

The results obtained using BET/BJH demonstrate that the metal-chitosan complexation synthesis method is highly efficient in obtaining materials with a porous structure in comparison with other methods used for the synthesis of aluminates. Wei and Chen [36], using the sol-gel method, obtained ZnAl_2O_4 with a surface area of $58 \text{ m}^2 \text{ g}^{-1}$ and pore volume of $0.0029 \text{ cm}^3 \text{ g}^{-1}$. Queiroz et al. [34] synthesized ZnAl_2O_4 using the polymeric precursor method and obtained a very low surface area ranging from 8 to $77 \text{ m}^2 \text{ g}^{-1}$ and a total pore volume ranging from 0.004 to $0.027 \text{ cm}^3 \text{ g}^{-1}$, respectively.

However, in the research carried out by Nuernberg et al. [21], MgAl_2O_4 synthesized using metal-chitosan complexation presented a surface area of $168 \text{ m}^2 \text{ g}^{-1}$ and $0.311 \text{ cm}^3 \text{ g}^{-1}$ of total pore volume, and such results contributed to better catalytic performance in the direct decomposition of methane. According to Anchieta et al. [15] high surface area and pore size are essential characteristics for catalytic purposes. In their research they obtained zinc aluminate with $158 \text{ m}^2 \text{ g}^{-1}$ and $0.302 \text{ cm}^3 \text{ g}^{-1}$ for surface area and total pore volume, respectively.

Faletto et al. [18] further demonstrated that ZnAl_2O_4 synthesized using different methods (co-precipitation, hydrothermal and micro-hydrothermal) alters the structural properties and that the pore size of the catalyst particles strongly influences the efficiency of the photocatalytic process in the degradation of textile dyes, like reactive red 141. Their results indicated that high photocatalytic activity was obtained for materials with larger pore sizes.

Thus, in this work, we note that the use of the metal-chitosan complexation method produced catalysts with larger pore size and volume and high surface area, as shown by the BET/BJH results. Such characteristics can probably contribute to a better photocatalytic performance.

3.7. Thermogravimetric Analysis (TG) and Differential Thermal Analysis (DTA)

The chitosan-aluminum-cobalt (QT-Al-Co) and chitosan-aluminum-nickel (QT-Al-Ni) samples submitted to thermogravimetric analysis under synthetic air and nitrogen gas atmosphere, available in Figure 6, presented three distinct events of weight loss (Figures S3 and S4). For the samples submitted to synthetic air, the first event occurred in the temperature range of 75 to $114 \text{ }^\circ\text{C}$ for the cobalt containing

sample and from 74 to 105 °C for the nickel complex. This event can be attributed to the loss of adsorbed water and the elimination of physically adsorbed gases from the sample surface.

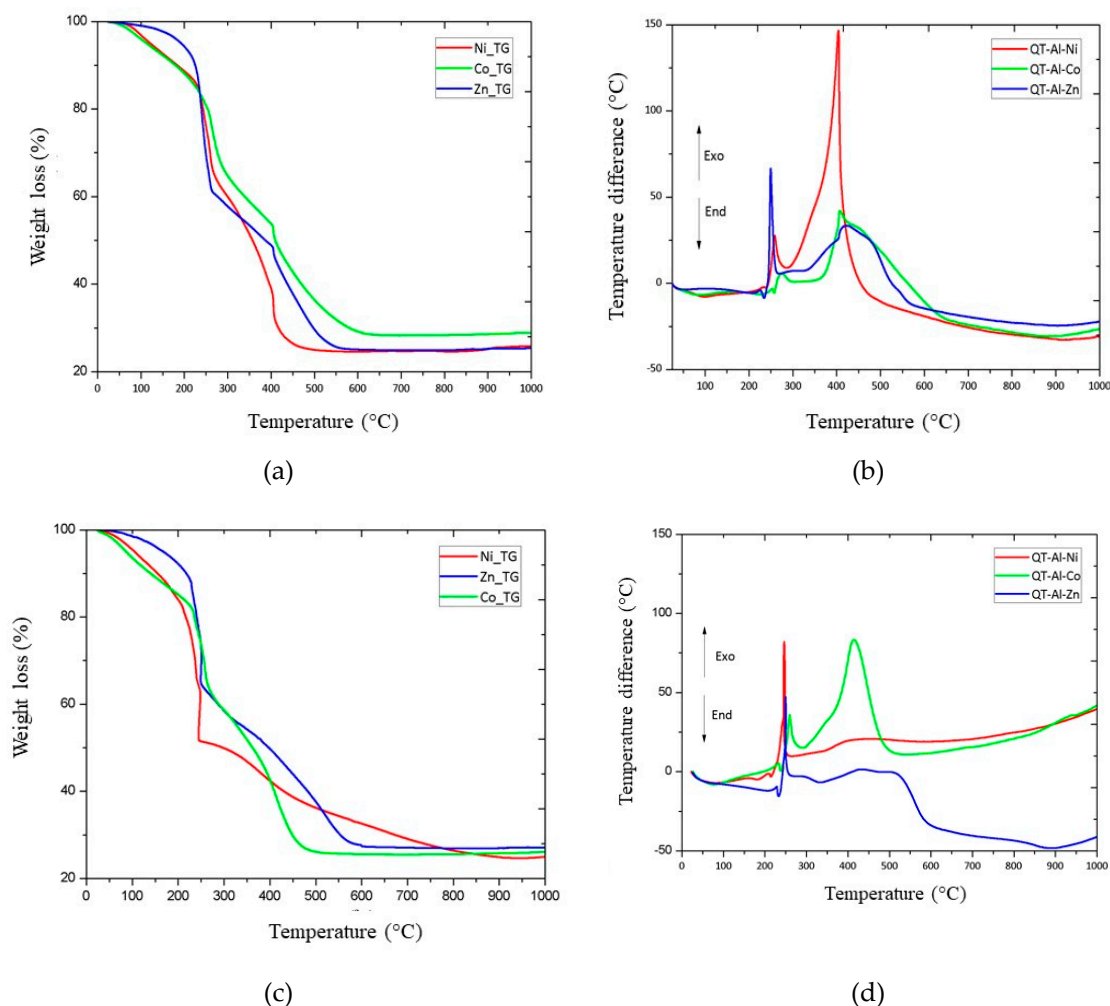


Figure 6. Thermogravimetric analysis of the samples QT-Al-Zn, QT-Al-Ni and QT-Al-Co under (a) air and (c) nitrogen. Differential thermal analysis for QT-Al-Zn, QT-Al-Ni and QT-Al-Co samples under (b) air and (d) nitrogen. Obtained in the temperature range of approximately 24 to 1000 °C, with a heating rate of 10 °C min⁻¹ and synthetic air flow of 50 mL min⁻¹.

For the chitosan-aluminum-cobalt complex this loss was 7.0%, for the chitosan-aluminum-nickel complex this loss reached 11.4%. However, the sample formed by the chitosan-aluminum-zinc complex showed no losses at this temperature [11,26].

By switching the purge gas to nitrogen, the TG curves showed a similar degradation profile. QT-Al-Co and QT-Al-Ni samples showed three events. QT-Al-Co presented the first event regarding the elimination of adsorbed water in the range of 71 to 105 °C with a weight loss of 5.8%. The QT-Al-Ni sample showed 14.4% of weight loss in the range of 44 to 110 °C. The QT-Al-Zn sample did not present this event regarding the loss of water and adsorbed gases.

The second event is related to the thermal deterioration of the nitrate-eliminating carbon chain (NO_x), which should occur in the range of 200 to 300 °C and is due to partial deterioration of chitosan [37,38]. In QT-Al-Zn, the first event, degradation, began at 213 °C and continued to 357 °C producing a 36.1% weight loss. QT-Al-Ni showed a weight loss of 27.9%, starting at a temperature of 238 °C and completing at 263 °C. The QT-Al-Co sample presented a 34.8% weight loss from 239 to 352 °C, when submitted to synthetic air atmosphere. When using nitrogen gas, QT-Al-Zn presented

the first event with a weight loss of 43.1% in the range of 243 to 250 °C. QT-Al-Co showed thermal degradation of 42.9% in the temperature range of 215 to 261 °C, while the QT-Al-Ni sample had a weight loss of 32.3% in the temperature range of 230 to 260 °C.

The third event was attributed to the total burning of charred waste that normally occurs between 400 and 600 °C [39,40]. For this event, the start and end temperatures were 371 and 414 °C, 379 and 506 °C and 213 and 561 °C for QT-Al-Ni, QT-Al-Co and QT-Al-Zn, respectively. The weight loss was 29.6% for QT-Al-Co, 38.5% for QT-Al-Ni and 35.7% for QT-Al-Zn. For the QT-Al-Ni, QT-Al-Co and QT-Al-Zn samples, submitted to nitrogen gas atmosphere, they presented a weight loss of 26.9%, 25.8% and 29.4% respectively. This event occurred in the range of 386 to 549 °C for the nickel-containing sample, for QT-Al-Co samples it was processed in the range of 325 to 596 °C and for the QT-Al-Zn samples it occurred in the range of 315 to 600 °C.

3.8. Photocatalytic Performance

According to Figure 7, a difference in the dye degradation rate can be observed as the calcination temperature of the $ZnAl_2O_4$ samples changed. Samples $ZnAl_2O_4$ -550, $ZnAl_2O_4$ -650, $ZnAl_2O_4$ -750, $ZnAl_2O_4$ -850 and $ZnAl_2O_4$ -950, Figure 7a, had a removal rate of 59%, 56%, 48%, 47% and 15%, respectively, at a reaction time of 150 min. The greatest separation between degradation rates occurred within 90 min from the beginning of the photocatalytic test, where a degradation of about 27%, 37%, 53%, 38% and 6% of the dye was observed for calcined zinc aluminate at temperatures of 550, 650, 750, 850 and 950 °C, respectively.

For the $Ni_{0.1}Zn_{0.9}Al_2O_4$ -950, $Ni_{0.5}Zn_{0.5}Al_2O_4$ -950, $Ni_{0.9}Zn_{0.1}Al_2O_4$ -950 and $NiAl_2O_4$ -950 samples, presented in Figure 7c, the samples $Ni_{0.1}Zn_{0.9}Al_2O_4$ -950, $Ni_{0.5}Zn_{0.5}Al_2O_4$ -950, $Ni_{0.9}Zn_{0.1}Al_2O_4$ -950 and $NiAl_2O_4$ -950 showed a removal rate of 64%, 51%, 55% and 66%.

The zinc aluminate samples replaced by Co^{2+} ions, presented in Figure 7b, showed a 83% removal for $Co_{0.1}Zn_{0.9}Al_2O_4$ -750, 63% for $Co_{0.5}Zn_{0.5}Al_2O_4$ -750 and 73% for $Co_{0.9}Zn_{0.1}Al_2O_4$ -750, and the $CoAl_2O_4$ -750 sample presented a degradation rate of 35% of rhodamine B dye. The highest degradation rate between the dyes was observed at 120 min reaction time with an 83%, 36%, 57% and 23% rate for samples replaced with 0.1, 0.5, 0.9 and 1.0 mol cobalt, respectively. Table 4 presents the rhodamine B dye removal rates for all photocatalysts evaluated.

Table 4. Degradation rate constant (k) and rhodamine B dye removal rate.

| Sample | Removal (%) | $k \text{ (min}^{-1}) \times 10^{-3}$ | R^2 |
|--------------------------------|-------------|---------------------------------------|-------|
| Blank | 13 | — | — |
| $ZnAl_2O_4$ -550 | 59 | 2.0 | 0.944 |
| $ZnAl_2O_4$ -650 | 56 | 3.3 | 0.972 |
| $ZnAl_2O_4$ -750 | 48 | 4.6 | 0.971 |
| $ZnAl_2O_4$ -850 | 47 | 1.8 | 0.946 |
| $ZnAl_2O_4$ -950 | 15 | 0.9 | 0.880 |
| $NiAl_2O_4$ -750 | 66 | 3.8 | 0.947 |
| $CoAl_2O_4$ -950 | 35 | 2.5 | 0.940 |
| $Ni_{0.1}Zn_{0.9}Al_2O_4$ -950 | 64 | 3.3 | 0.855 |
| $Ni_{0.5}Zn_{0.5}Al_2O_4$ -950 | 51 | 5.1 | 0.936 |
| $Ni_{0.9}Zn_{0.1}Al_2O_4$ -950 | 55 | 2.3 | 0.931 |
| $Co_{0.1}Zn_{0.9}Al_2O_4$ -750 | 83 | 4.9 | 0.975 |
| $Co_{0.5}Zn_{0.5}Al_2O_4$ -750 | 62 | 4.8 | 0.957 |
| $Co_{0.9}Zn_{0.1}Al_2O_4$ -750 | 73 | 2.9 | 0.954 |

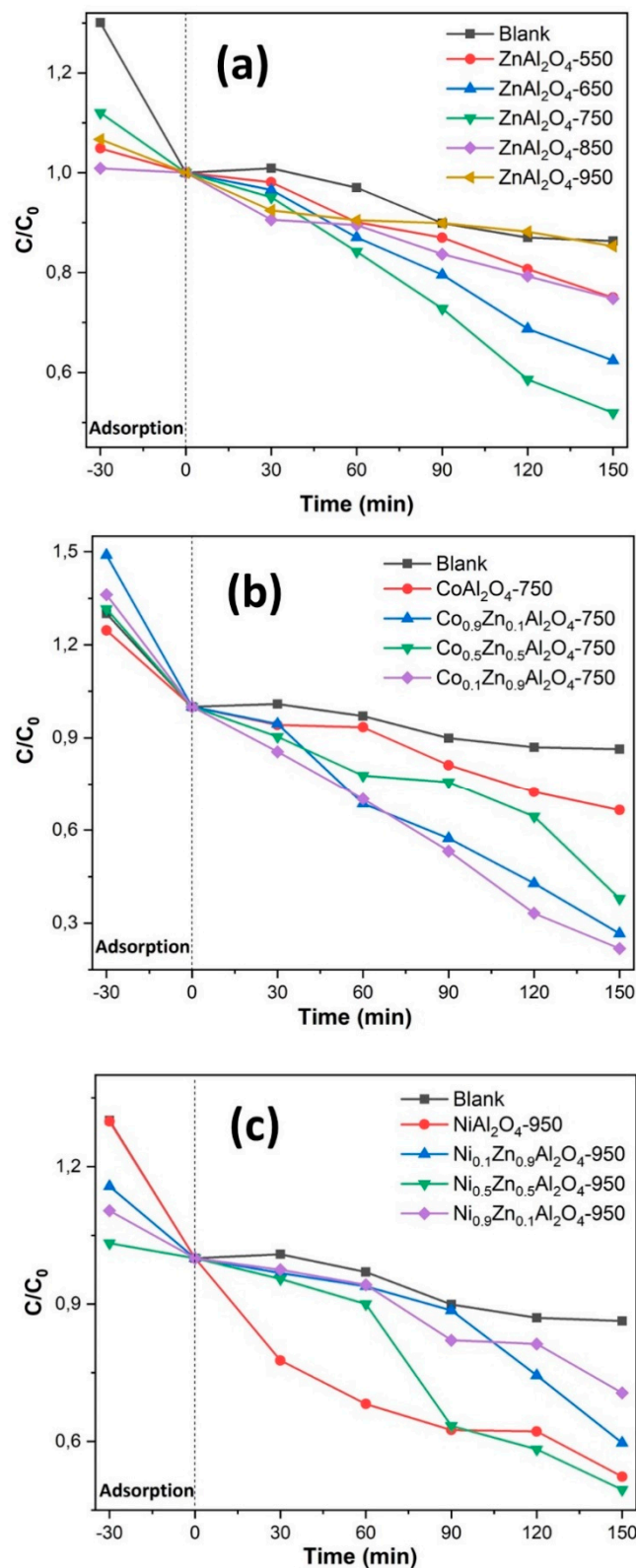
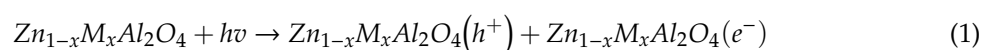


Figure 7. Rhodamine B photocatalytic degradation test for samples: ZnAl₂O₄-550, ZnAl₂O₄-650, ZnAl₂O₄-750, ZnAl₂O₄-850, ZnAl₂O₄-950 (a); CoAl₂O₄-750, Co_{0.1}Zn_{0.9}Al₂O₄-750, Co_{0.5}Zn_{0.5}Al₂O₄-750, Co_{0.9}Zn_{0.1}Al₂O₄-750 (b); NiAl₂O₄-950, Ni_{0.1}Zn_{0.9}Al₂O₄-950, Ni_{0.5}Zn_{0.5}Al₂O₄-950, Ni_{0.9}Zn_{0.1}Al₂O₄-950 (c) and blank (direct photolysis).

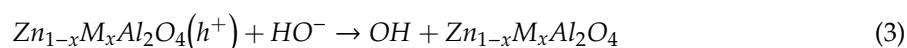
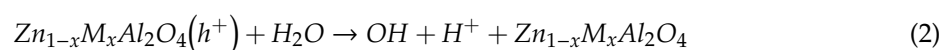
The increase in the removal rate of zinc aluminate substituted by 0.1 cobalt ions may be justified by the decrease of bandgap energy, material, and its high surface area, in relation to unsubstituted samples. However, the nickel ion-replaced samples did not show a significant increase in the degradation rate, and this may be attributed to the fact that the substitution did not cause significant changes in bandgap, but also the fact that the high synthesis temperature reduced the surface area of the samples. The degradation rate for rhodamine B dye using photolysis were 13% after 150 min under ultraviolet radiation exposure. Ragul and Sumathi [41] reported a degradation rate of 20% using pure zinc aluminate as a photocatalyst when degrading rhodamine B dye.

In the photodegradation process, the photocatalyst promotes a variety of photoinduced chemical reactions that occur in the presence of O_2 and H_2O , and the products formed are capable of promoting the degradation of organic pollutants [42]. In the literature, the $ZnAl_2O_4$ bandgap is theoretically reported to be 3.8 eV; however, some studies report a bandgap greater than 5.0 eV. Therefore, ultraviolet light becomes necessary to activate the photocatalyst [3,42].

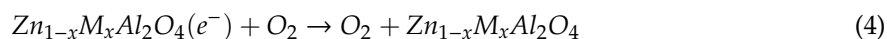
The following diagram shows the events that can occur on the surface of $Zn_{1-x}M_xAl_2O_4$ ($M = Co^{2+}, Ni^{2+}$) until photodegradation of rhodamine B [43–45]. When light is absorbed by $Zn_{1-x}M_xAl_2O_4$ ($M = Co^{2+}, Ni^{2+}$) two charge carriers are generated, electrons (e^-) and positive holes (h^+).



The photogenerated holes can react with water (Equation (2)) and with hydroxide ions that are adsorbed on the surface of the material producing hydroxyl radical (Equation (3)).



The electrons formed in the process of excitation with radiation react with the dissolved molecular oxygen forming superoxide anions (Equation (4)) followed by the protonation of the superoxide (Equation (5)).



When the photocatalytic decomposition process is complete, the photo-generated radicals promote the complete decomposition of the organic pollutant in carbon dioxide and water (Equation (6)).



3.9. Kinetic Degradation Studies

The photodegradation reactions of organic pollutants follow first-order degradation kinetics. In this case, it is suggested that the degradation rate following pseudo-first-order kinetics can be explained using a Langmuir-Hinshelwood model [15,46]. As seen in Figure 8, the relationship between $-\ln(C/C_0)$ demonstrates that the degradation of rhodamine B catalyzed by most of the synthesized photocatalysts agrees with pseudo-first-order kinetics.

The photodegradation rate (r) of rhodamine B after the adsorption equilibrium can be expressed by Equation (7):

$$\ln(C/C_0) = -kt \quad (7)$$

where C_0 is the initial concentration of the solution after reaching the adsorption equilibrium, C is the concentration at time t , and k is the reaction rate constant for the photodegradation process [7,47].

Table 4 presents the values of the degradation rate constant (k) and the rhodamine B dye removal rate. With these values, it can be concluded that the dye photodegradation process for most of the photocatalysts in question follows pseudo-first-order kinetics.

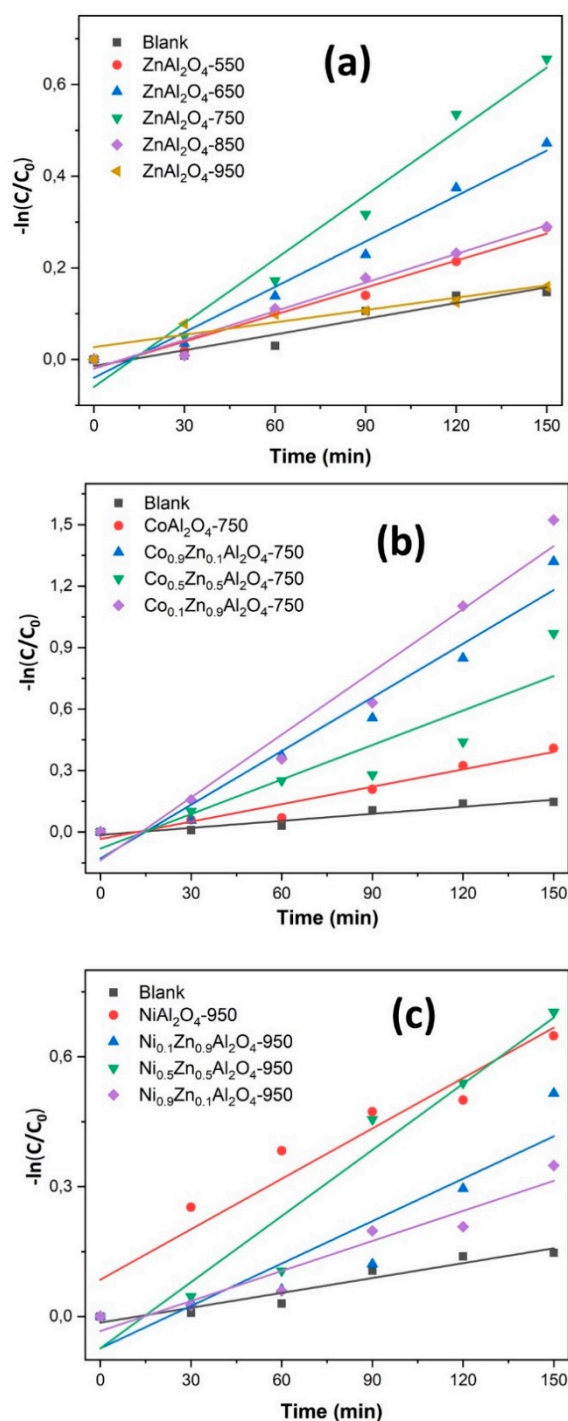


Figure 8. Rhodamine B photocatalytic degradation kinetics for samples: ZnAl₂O₄-550, ZnAl₂O₄-650, ZnAl₂O₄-750, ZnAl₂O₄-850, ZnAl₂O₄-950 (a); CoAl₂O₄-750, Co_{0.1}Zn_{0.9}Al₂O₄-750, Co_{0.5}Zn_{0.5}Al₂O₄-750, Co_{0.9}Zn_{0.1}Al₂O₄-750 (b); NiAl₂O₄-950, Ni_{0.1}Zn_{0.9}Al₂O₄-950, Ni_{0.5}Zn_{0.5}Al₂O₄-950, Ni_{0.9}Zn_{0.1}Al₂O₄-950 (c) and Blank (direct photolysis).

4. Conclusions

Zn_{1-x}M_xAl₂O₄ was successfully obtained using the metal-chitosan complexation method and Zn²⁺ ions were gradually replaced by Co²⁺ and Ni²⁺. XRD and FTIR analysis confirmed the formation of the spinel phase and the high degree of purity in all synthesized samples. Mesoporous Zn_{1-x}M_xAl₂O₄ was developed with a smaller band interval and a greater number of reaction sites available for rhodamine B photodegradation. Here, we investigated for the first time the photocatalytic activity

of $Zn_{1-x}M_xAl_2O_4$ obtained using metal-chitosan complexation method and the effect of replacing Zn^{2+} ions with Ni^{2+} and Co^{2+} on the degradation of rhodamine B. The photocatalytic activity was investigated under ultraviolet radiation. $ZnAl_2O_4$ -950 and $Co_{0.1}Zn_{0.9}Al_2O_4$ -750 samples had the lowest (15%) and highest (83%) dye degradation rates, respectively. Rhodamine B photodegradation followed pseudo-first-order kinetics.

Supplementary Materials: The following are available online at <http://www.mdpi.com/1996-1944/13/9/2150/s1>, Figure S1. Comparison between UV-Vis diffuse reflectance spectra of samples: $ZnAl_2O_4$ -550, $ZnAl_2O_4$ -650, $ZnAl_2O_4$ -750, $ZnAl_2O_4$ -850, $ZnAl_2O_4$ -950, Figure S2. Metal spheres complexed with chitosan before calcination: (a) QT-Zn-Al, (b) QT-Ni-Al, (c) QT-Co-Al, Figure S3. DTA and TG of pure chitosan in (a) synthetic air and (b) nitrogen under synthetic air atmosphere with a flow of $50\text{ cm}^3\text{ min}^{-1}$ and a heating ratio of $10\text{ }^\circ\text{C min}^{-1}$ to a temperature of $1000\text{ }^\circ\text{C}$, Figure S4. TG and DTG curves of pure chitosan in (a) synthetic air and (b) nitrogen gas with a flow of $50\text{ cm}^3/\text{min}$ and heating ratio of $10\text{ }^\circ\text{C}/\text{min}$ from $\sim 24\text{ }^\circ\text{C}$ to $700\text{ }^\circ\text{C}$.

Author Contributions: Conceptualization, G.N.d.R.F.; methodology, J.R.Z., L.A.S.d.N., C.E.F.d.C. and G.N.d.R.F.; formal analysis, N.M.P.d.N. and B.R.M.d.L.; investigation, N.M.P.d.N. and B.R.M.d.L.; resources, L.A.S.d.N., J.R.Z., C.E.F.d.C. and G.N.d.R.F.; data curation, J.R.Z., R.L. and G.N.d.R.F.; writing—original draft preparation, N.M.P.d.N. and B.R.M.d.L.; writing—review and editing, G.N.d.R.F., L.A.S.d.N. and R.L.; visualization, R.L., G.N.d.R.F. and L.A.S.d.N.; supervision, R.L., C.E.F.d.C., G.N.d.R.F.; project administration, G.N.d.R.F. and R.L.; funding acquisition, G.N.d.R.F. and L.A.S.d.N. All authors have read and agreed to the published version of the manuscript.

Funding: This research was funded by CNPQ, grant number 432221/2018-2 and Banco da Amazônia grant number 2018/212.

Acknowledgments: The authors are grateful to the PROPESP/Federal University of Pará, the Fuel Research and Analysis Laboratory, Laboratory of Oils of the Amazon (LOA), and the Laboratory of Catalysis and Oil Chemistry (LCO/UFGPA) where the research was developed. Thanks also to the High Pressure and Vibrational Spectroscopy Labs, the X-Ray Diffraction Lab and the Nanomanipulation Lab. This study was financed in part by the Coordenação de Aperfeiçoamento de Pessoal de Nível Superior (CAPES - Brazil), Finance Code 001.

Conflicts of Interest: The authors declare no conflicts of interest.

References

1. Chen, F.; Zhao, E.; Kim, T.; Wang, J.; Hableel, G.; Reardon, P.J.T.; Ananthakrishna, S.J.; Wang, T.; Arconada-Alvarez, S.; Knowles, J.C.; et al. Organosilica Nanoparticles with an Intrinsic Secondary Amine: An Efficient and Reusable Adsorbent for Dyes. *ACS Appl. Mater. Interfaces* **2017**, *9*, 15566–15576. [[CrossRef](#)] [[PubMed](#)]
2. Yin, J.; Zhu, Y.; Yue, X.; Wang, L.; Zhu, H.; Wang, C. From environmental pollutant to activated carbons for high-performance supercapacitors. *Electrochim. Acta* **2016**, *201*, 96–105. [[CrossRef](#)]
3. Liu, J.; Li, X.M.; He, J.; Wang, L.Y.; Lei, J. Du Combining the photocatalysis and absorption properties of core-shell Cu-BTC@TiO₂ microspheres: Highly efficient desulfurization of thiophenic compounds from fuel. *Materials* **2018**, *11*. [[CrossRef](#)] [[PubMed](#)]
4. Nakatsuka, A.; Ikeda, Y.; Yamasaki, Y.; Nakayama, N.; Mizota, T. Cation distribution and bond lengths in CoAl₂O₄ spinel. *Solid State Commun.* **2003**, *128*, 85–90. [[CrossRef](#)]
5. Kapse, S.D.; Raghuwanshi, F.C.; Kapse, V.D.; Patil, D.R. Characteristics of high sensitivity ethanol gas sensors based on nanostructured spinel Zn_{1-x}Co_xAl₂O₄. *Curr. Appl. Phys.* **2012**, *12*, 307–312. [[CrossRef](#)]
6. Mohaček-Grošev, V.; Vrankić, M.; Maksimović, A.; Mandić, V. Influence of titanium doping on the Raman spectra of nanocrystalline ZnAl₂O₄. *J. Alloys Compd.* **2017**, *697*, 90–95. [[CrossRef](#)]
7. Atkins, P.W.; Paula, J. *Physical Chemistry: Vol 2*, 9th ed.; Silva Edilson, C.D., Cardoso Márcio, J.E.M., Barcia Osvaldo, E., Eds.; LTC: Rio de Janeiro, Brazil, 2013; ISBN 9788521621058.
8. Gómez-Solís, C.; Peralta-Arriaga, S.L.; Torres-Martínez, L.M.; Juárez-Ramírez, I.; Díaz-Torres, L.A. Photocatalytic activity of MAl₂O₄ (M = Mg, Sr and Ba) for hydrogen production. *Fuel* **2017**, *188*, 197–204. [[CrossRef](#)]
9. Khademolhoseini, S.; Talebi, R. Green synthesis and characterization of cobalt aluminate nanoparticles and its photocatalyst application. *J. Mater. Sci. Mater. Electron.* **2016**, *27*, 2938–2943. [[CrossRef](#)]
10. Battiston, S.; Rigo, C.; Da Cruz Severo, E.; Mazutti, M.A.; Kuhn, R.C.; Gündel, A.; Foletto, E.L. Synthesis of zinc aluminate (ZnAl₂O₄) Spinel and its application as photocatalyst. *Mater. Res.* **2014**, *17*, 734–738. [[CrossRef](#)]

11. Souza, L.K.C.; De Ange, S.; Carlos, E.F.; Souza, A.G.; Scheller, T. Blue pigments based on $\text{Co}_x\text{Zn}_{1-x}\text{Al}_2\text{O}_4$ spinels synthesized by the polymeric precursor method. *Dye. Pigment.* **2009**, *81*, 187–192. [[CrossRef](#)]
12. Anand, G.T.; Kennedy, L.J.; Vijaya, J.J. Microwave combustion synthesis, structural, optical and magnetic properties of $\text{Zn}_{1-x}\text{Co}_x\text{Al}_2\text{O}_4$ ($0 \leq x \leq 0.5$) spinel nanostructures. *J. Alloys Compd.* **2013**, *581*, 558–566. [[CrossRef](#)]
13. Duan, X.; Yuan, D.; Yu, F. Cation distribution in Co-doped ZnAl_2O_4 nanoparticles studied by X-ray photoelectron spectroscopy and ^{27}Al solid-state NMR spectroscopy. *Inorg. Chem.* **2011**, *50*, 5460–5467. [[CrossRef](#)] [[PubMed](#)]
14. Šepelák, V.; Becker, K.D. Comparison of the cation inversion parameter of the nanoscale milled spinel ferrites with that of the quenched bulk materials. *Mater. Sci. Eng. A* **2004**, 375–377, 861–864. [[CrossRef](#)]
15. Anchieta, C.G.; Sallet, D.; Foletto, E.L.; Da Silva, S.S.; Chiavone-Filho, O.; Do Nascimento, C.A.O. Synthesis of ternary zinc spinel oxides and their application in the photodegradation of organic pollutant. *Ceram. Int.* **2014**, *40*, 4173–4178. [[CrossRef](#)]
16. Hassanzadeh-Tabrizi, S.A.; Pournajaf, R.; Moradi-Faradonbeh, A.; Sadeghinejad, S. Nanostructured CuAl_2O_4 : Co-precipitation synthesis, optical and photocatalytic properties. *Ceram. Int.* **2016**, *42*, 14121–14125. [[CrossRef](#)]
17. Yanyan, J.; Jinggang, L.; Xiaotao, S.; Guiling, N.; Chengyu, W.; Xiumei, G. CuAl_2O_4 powder synthesis by sol-gel method and its photodegradation property under visible light irradiation. *J. Sol-Gel Sci. Technol.* **2007**, *42*, 41–45. [[CrossRef](#)]
18. Foletto, E.L.; Battiston, S.; Simões, J.M.; Bassaco, M.M.; Pereira, L.S.F.; De Moraes Flores, É.M.; Müller, E.I. Synthesis of ZnAl_2O_4 nanoparticles by different routes and the effect of its pore size on the photocatalytic process. *Microporous Mesoporous Mater.* **2012**, *163*, 29–33. [[CrossRef](#)]
19. Moro, C.C.; Lansarin, M.A.; Bagnara, M. Nitrogen-doped TiO_2 nanotubes: Comparison of photocatalytic activities of materials obtained using different techniques. *Quim. Nova* **2012**, *35*, 1560–1565. [[CrossRef](#)]
20. Liu, G.; Han, C.; Pelaez, M.; Zhu, D.; Liao, S.; Likodimos, V.; Ioannidis, N.; Kontos, A.G.; Falaras, P.; Dunlop, P.S.M.; et al. Synthesis, characterization and photocatalytic evaluation of visible light activated C-doped TiO_2 nanoparticles. *Nanotechnology* **2012**, *23*. [[CrossRef](#)]
21. Nuernberg, G.B.; Foletto, E.L.; Probst, L.F.D.; Carreño, N.L.V.; Moreira, M.A. MgAl_2O_4 spinel particles prepared by metal-chitosan complexation route and used as catalyst support for direct decomposition of methane. *J. Mol. Catal. A Chem.* **2013**, *370*, 22–27. [[CrossRef](#)]
22. Naderi, M.; Shamirian, A.; Edrisi, M. Synthesis, characterization and photocatalytic properties of nanoparticles CuAl_2O_4 by Pechini method using Taguchi statistical design. *J. Sol-Gel Sci. Technol.* **2011**, *58*, 557–563. [[CrossRef](#)]
23. Zeng, L.; Lu, Z.; Li, M.; Yang, J.; Song, W.; Zeng, D.; Xie, C. A modular calcination method to prepare modified N-doped TiO_2 nanoparticle with high photocatalytic activity. *Appl. Catal. B Environ.* **2016**, *183*, 308–316. [[CrossRef](#)]
24. Nuernberg, G.D.B.; Foletto, E.L.; Probst, L.F.D.; Campos, C.E.M.; Carreño, N.L.V.; Moreira, M.A. A novel synthetic route for magnesium aluminate (MgAl_2O_4) particles using metal-chitosan complexation method. *Chem. Eng. J.* **2012**, *193*, 211–214. [[CrossRef](#)]
25. Stringhini, F.M.; Foletto, E.L.; Sallet, D.; Bertuol, D.A.; Chiavone-Filho, O.; Nascimento, C.A.O. Do Synthesis of porous zinc aluminate spinel (ZnAl_2O_4) by metal-chitosan complexation method. *J. Alloys Compd.* **2014**, *588*, 305–309. [[CrossRef](#)]
26. He, Z.; Sun, C.; Yang, S.; Ding, Y.; He, H.; Wang, Z. Photocatalytic degradation of rhodamine B by Bi_2WO_6 with electron accepting agent under microwave irradiation: Mechanism and pathway. *J. Hazard. Mater.* **2009**, *162*, 1477–1486. [[CrossRef](#)]
27. Zhu, Z.; Wang, Z.; Di, J.; Long, Y.; Li, W. Enhanced visible-light photocatalytic properties of g- C_3N_4 by coupling with ZnAl_2O_4 . *Catal. Commun.* **2016**, *86*, 86–90. [[CrossRef](#)]
28. Han, Y.S.; Li, J.B.; Ning, X.S.; Chi, B. Effect of preparation temperature on the lattice parameter of nickel aluminate spinel. *J. Am. Ceram. Soc.* **2004**, *87*, 1347–1349. [[CrossRef](#)]
29. Porta, P.; Anichini, A.; Bucciarelli, U. Distribution of nickel ions among octahedral and tetrahedral sites in $\text{Ni}_x\text{Zn}_{1-x}\text{Al}_2\text{O}_4$ spinel solid solutions. *J. Chem. Soc. Faraday Trans. 1 Phys. Chem. Condens. Phases* **1979**, *75*, 1876–1887. [[CrossRef](#)]

30. Ianoş, R.; Lazău, R.; Lazău, I.; Păcurariu, C. Chemical oxidation of residual carbon from ZnAl₂O₄ powders prepared by combustion synthesis. *J. Eur. Ceram. Soc.* **2012**, *32*, 1605–1611. [[CrossRef](#)]
31. Dhak, D.; Pramanik, P. Particle size comparison of soft-chemically prepared transition metal (Co, Ni, Cu, Zn) aluminate pinels. *J. Am. Ceram. Soc.* **2006**, *89*, 1014–1021. [[CrossRef](#)]
32. Gama, L.; Ribeiro, M.A.; Barros, B.S.; Kiminami, R.H.A.; Weber, I.T.; Costa, A.C.F.M. Synthesis and characterization of the NiAl₂O₄, CoAl₂O₄ and ZnAl₂O₄ spinels by the polymeric precursors method. *J. Alloys Compd.* **2009**, *483*, 453–455. [[CrossRef](#)]
33. Porta, P.; Stone, F.S.; Turner, R.G. The distribution of nickel ions among octahedral and tetrahedral sites in NiAl₂O₄MgAl₂O₄ solid solutions. *J. Solid State Chem.* **1974**, *11*, 135–147. [[CrossRef](#)]
34. Queiroz, R.M.; Coelho, T.L.; Queiroz, I.M.; Pires, L.H.O.; Santos, I.M.G.; Zamian, J.R.; da Rocha Filho, G.N.; da Costa, C.E.F. Structural and thermal characterization of Ni_xZn_{1-x}Al₂O₄ synthesized by the polymeric precursor method. *J. Therm. Anal. Calorim.* **2016**, *124*, 1023–1028. [[CrossRef](#)]
35. Sing, K.S.W.; Everett, D.H.; Haul, R.A.W.; Moscou, L.; Pierotti, A.R.; Rouquérol, J.; Siemieniewska, T. Reporting Physisorption Data for Gas/Solid Systems including catalysis * reporting physisorption data for gas/solid systems with Special Reference to the Determination of Surface Area and Porosity. *Pure Appl. Chem.* **1985**, *57*, 603–619. [[CrossRef](#)]
36. Wei, X.; Chen, D. Synthesis and characterization of nanosized zinc aluminate spinel by sol-gel technique. *Mater. Lett.* **2006**, *60*, 823–827. [[CrossRef](#)]
37. Braga, T.P.; Longhinotti, E.; Pinheiro, A.N.; Valentini, A. Synthesis of hybrid spheres for the dehydrogenation of ethylbenzene in the presence of CO₂. *Appl. Catal. A Gen.* **2009**, *362*, 139–146. [[CrossRef](#)]
38. Jiang, R.; Zhu, H.Y.; Chen, H.H.; Yao, J.; Fu, Y.Q.; Zhang, Z.Y.; Xu, Y.M. Effect of calcination temperature on physical parameters and photocatalytic activity of mesoporous titania spheres using chitosan/poly(vinyl alcohol) hydrogel beads as a template. *Appl. Surf. Sci.* **2014**, *319*, 189–196. [[CrossRef](#)]
39. Gabal, M.A.; Kosa, S.; Almutairi, T.S. Cr-substitution effect on the structural and magnetic properties of nano-sized NiFe₂O₄ prepared via novel chitosan route. *J. Magn. Magn. Mater.* **2014**, *356*, 37–41. [[CrossRef](#)]
40. Briceño, S.; Suarez, J.; Gonzalez, G. Solvothermal synthesis of cobalt ferrite hollow spheres with chitosan. *Mater. Sci. Eng. C* **2017**, *78*, 842–846. [[CrossRef](#)]
41. Ragul, G.; Sumathi, S. Synthesis, characterization and photocatalytic study of zinc aluminate nanopowders against Rhodamine-B and crystal violet dyes. *Int. J. Appl. Eng. Res.* **2013**, *8*, 2175–2178.
42. Augugliaro, V.; Loddo, V.; Pagliaro, M.; Palmisano, G.; Palmisano, L. *Clean by Light Irradiation: Practical Applications of Supported TiO₂—Fundamentals Chapter 1*, 1st ed.; Royal Society of Chemistry: London, UK, 2010; pp. 1–40. ISBN 9781849732031. [[CrossRef](#)]
43. Campos, W.E.O.; Nobre, F.X.; Filho, G.N.R.; Silva, M.A.R.; Costa, C.E.F.; Nascimento, L.A.S.; Zamian, J.R. High Photocatalytic Activity under Visible Light for a New Morphology of Bi₂WO₆ Microcrystals. *Catalysts* **2019**, *9*, 667. [[CrossRef](#)]
44. Younas, H.; Qazi, I.A.; Hashmi, I.; Ali Awan, M.; Mahmood, A.; Qayyum, H.A. Visible light photocatalytic water disinfection and its kinetics using Ag-doped titania nanoparticles. *Environ. Sci. Pollut. Res.* **2014**, *21*, 740–752. [[CrossRef](#)] [[PubMed](#)]
45. Sandip, Q. Efficient adsorption and photocatalytic degradation of Rhodamine B dye over Bi₂O₃-bentonite nanocomposites: A kinetic study. *J. Ind. Eng. Chem.* **2015**, *34*, 356–363.
46. Gaya, U.I. *Heterogeneous Photocatalysis Using Inorganic Semiconductor Solid*; Springer: London, UK, 2013; ISBN 978-94-007-7775-0.
47. Zhao, X.; Wang, Z.; Zhang, C.; Yuan, S.; Zhu, Y.; Wang, J. Fabrication and Photocatalytic Properties of Novel ZnO/ZnAl₂O₄ Nanocomposite with ZnAl₂O₄ Dispersed Inside ZnO Network. *AIChE J.* **2012**, *59*, 215–228. [[CrossRef](#)]

